Experimental and Computational Investigation of Lanthanide Ion Doping on $BiVO_4$ Photoanodes for Solar Water Splitting

Gokul V. Govindaraju,[1,†] Juliana M. Morbec,[2,†,§] Giulia A. Galli,[2,3,4*] and Kyoung-Shin Choi[1,*]

[1]*Department of Chemistry, University of Wisconsin-Madison, Madison, Wisconsin 53706, United States*

[2]*Institute for Molecular Engineering, University of Chicago, Chicago, Illinois 60637*

[3]*Department of Chemistry, University of Chicago, Chicago, Illinois 60637*

[4]*Materials Science Division, Argonne National Laboratory, Lemont, Illinois*

[†] These authors contributed equally.

[§] Current address: Faculty of Physics, University of Duisburg-Essen, Lotharstrasse 1, 47057 Duisburg, Germany

* Correspondence and requests for materials should be addressed to K.-S.C. (email: kschoi@chem.wisc.edu) and G.A.G. (email: gagalli@uchicago.edu).

ABSTRACT

N-Type bismuth vanadate ($BiVO_4$) has emerged as one of the most promising photoanodes for use in water splitting photoelectrochemical cells in recent years. However, its photoelectrochemical properties may be further enhanced by optimizing its bandgap and its charge transport properties. Doping at the V^{5+} and O^{2-} sites of $BiVO_4$ has proven to be an effective strategy to alter the oxide electronic band structure and/or charge transport properties, but the effect of doping at the Bi^{3+} site is not nearly as well understood. In this study, we performed a combined experimental and theoretical study of $BiVO_4$ doped with lanthanide (Ln) elements (La, Ce, Sm, and Yb) at the Bi^{3+} site, and we elucidated the effect of doping on the electronic band structure and charge transport properties of $BiVO_4$. Furthermore, we performed density-functional theory calculations to investigate the combined effect of the Ln doping and oxygen vacancies, which are intrinsic defects in $BiVO_4$. Our results showed that for some cases the simultaneous consideration of Ln doping and O vacancy leads to changes that cannot be obtained by the sum of the changes caused by Ln doping alone and O vacancy alone, which was critical to understanding the experimental results. The various ways that the Ln dopants modified the electronic band structure and charge transport properties of $BiVO_4$ demonstrated in this study can provide useful guidelines for the tuning of the composition of oxide-based photoelectrodes.

1. Introduction

Practical solar hydrogen production using water splitting photoelectrochemical cells (PECs) critically depends on the cost of solar hydrogen production.[1-3] One of the approaches to lowering the production cost of solar hydrogen production is the development of oxide-based polycrystalline semiconductors for use as photoelectrodes in a PEC device, due to generally cheaper costs of the raw materials and of electrode processing.[4-5] Among oxide-based semiconductors, n-type monoclinic bismuth vanadate ($BiVO_4$) has emerged as a promising candidate for use as a photoanode in PECs.[6-7] When fabricated as polycrystalline electrodes, $BiVO_4$ is shown not to suffer from serious bulk and surface electron-hole recombination unlike other oxide-based photoelectrodes.[7-10] Also, $BiVO_4$ possesses favorable conduction band and valence band positions for the water splitting reaction while having a bandgap that can absorb visible light.[6, 11] Furthermore, its photostability for solar water splitting when paired with proper oxygen evolution catalysts has recently been demonstrated for several hundred hours, confirming the promise of $BiVO_4$ for sustainable PEC operation.[12-13]

Based on these promising features, various doping studies have been performed to date to further enhance the photoelectrochemical properties of monoclinic $BiVO_4$ via composition tuning. Most commonly reported doping studies involve the modification of the vanadium site. For example, doping Mo^{6+} and W^{6+} ions on the V^{5+} site is known to increase the majority carrier density, which improves the electron transport properties and electron-hole separation.[14-17] In addition, several studies on manipulating the oxygen site of $BiVO_4$ have been reported. For example, increasing oxygen vacancies in the $BiVO_4$ lattice by annealing under a reducing environment (e.g. under H_2 or N_2 flow) was shown to improve the majority carrier density of

$BiVO_4$.[18-20] Recently, it was also demonstrated that replacing oxygen with nitrogen can decrease the bandgap of $BiVO_4$ while improving its charge transport properties.[21]

Compared to investigations of vanadium and oxygen sites of monoclinic $BiVO_4$, studies on the composition tuning of Bi sites have been relatively empirical; although changes in properties were reported after Bi-site doping, no elucidations have been made regarding how the dopants caused the observed modifications.[22-26] To accurately elucidate the doping effect on the Bi site, confirmation of dopant incorporation in the lattice must be obtained first, so as to exclude the case of dopants accumulating at the surface. Another important prerequisite for a rigorous doping study is to ensure that the pristine and doped samples have comparable morphologies. If dopants added during the synthesis resulted in a change of morphology, it would be difficult to unambiguously determine the reason for the observed difference between the pristine and doped samples.

In this study, we report experimental and computational investigations of doping lanthanide ions (Ln: La, Ce, Sm, Yb) at the Bi sites of $BiVO_4$. The trivalent Ln ions have similar ionic size and coordination preference to those of Bi^{3+}. Therefore, they are expected to substitutionally replace Bi^{3+} in the $BiVO_4$ lattice. While +3 is the most stable oxidation state for most Ln ions, some are also known to have mixed valencies depending on their structural and chemical environment (e.g. $Ce^{3+/4+}$, $Sm^{2+/3+}$, and $Yb^{2+/3+}$). Therefore, it is possible that these ions may exert different effects on the charge transport properties of $BiVO_4$, which are interesting to systematically elucidate. In order to satisfy the aforementioned requirements for meaningful doping studies, we identified synthesis conditions to prepare pristine and Ln-doped samples with comparable morphologies. Furthermore, the incorporation of Ln ions into the Bi site could be

unambiguously confirmed by X-ray diffraction that showed changes in cell parameters according to the size of the dopant ions incorporated in the $BiVO_4$ lattice.

Although lanthanide ions are known to have similar bonding natures and show similar chemistry, the lanthanide ions selected in this study exhibited different effects on the electronic band structure of $BiVO_4$. In addition to the effect of Ln doping, we also investigated how these dopants interact with oxygen vacancies, a common defect of $BiVO_4$. We demonstrate that understanding of the combined effect of lanthanide doping and oxygen vacancies is critical to accurately interpret the measured photoelectrochemical properties of lanthanide doped $BiVO_4$ photoelectrodes.

2. Experimental

Synthesis of Lanthanide-doped $BiVO_4$.

$BiVO_4$ was prepared by first electrodepositing precursor BiOI electrodes on a fluorine-doped tin oxide (FTO) working electrode, as described in previous reports.[7, 27] The BiOI electrodes were converted to $BiVO_4$ electrodes by annealing at 450 °C for 2 h in the air (ramping rate =1.8 °C/min) after covering the electrode surface (lateral dimensions of the BiOI electrode = 1 cm x 1.25 cm) with 75 μL of a dimethyl sulfoxide (DMSO) solution containing 0.15 M vanadyl acetylacetonate ($VO(acac)_2$). Excess V_2O_5 present in the $BiVO_4$ electrodes was removed by soaking the electrodes in 1 M KOH solution for 30 min with gentle stirring. The resultant Ln-$BiVO_4$ films were rinsed in DI water and dried under a gentle N_2 flow.

In order to produce Ln-doped $BiVO_4$, the BiOI electrodes were annealed using the above conditions after a 0.15 M $VO(acac)_2$ DMSO solution containing varying amounts of lanthanide nitrate precursors ($La(NO_3)_3$, $Ce(NO_3)_3$, $Sm(NO_3)_3$, and $Yb(NO_3)_3$) was added on the top. An

optimum concentration of the La, Ce, Sm and Yb precursors was 0.00075 M in the DMSO solution, which resulted in the production of $BiVO_4$ films that contain 2.5-3.0% Ln ions in the V site.. After the synthesis, some lanthanide oxides were present in the edge area of the Ln-doped $BiVO_4$ electrodes, which was due to the lanthanide ions being concentrated in the edge of the drop-casted DMSO solution during annealing. However, they did not affect the characterization of the Ln-doped $BiVO_4$ electrodes, which was carried out using only the central region of the electrodes while masking the rest.

Characterization.

The purity and crystal structure of $BiVO_4$ and Ln-doped $BiVO_4$ were examined by powder X-ray diffraction (Bruker D8 Advanced PXRD, λ = 1.5418 Å, 298 K, Ni-filtered Cu K_α radiation. The morphology of the synthesized electrodes was examined with a scanning electron microscope (LEO 1530) operated at an accelerating voltage of 2 kV. The atomic composition of Ln-doped $BiVO_4$ was measured with a Thermo Fisher UltraDry EDS detector attached to the LEO 1530 scanning electron microscope at an accelerating voltage of 15 kV. Multiple locations of the multiple samples obtained by each synthesis condition were analyzed to confirm a consistent average composition. Ultraviolet-visible absorption spectra were obtained on an Agilent Cary 5000 spectrophotometer in which the sample was placed in the center of an integrating sphere to accurately assess the absorbance. X-ray photoelectron spectroscopy spectra were obtained using a Thermo Scientific K-Alpha X-ray photoelectron spectrometer with an Al Kα excitation source. The binding energies were calibrated with respect to the residual carbon 1s peak at 284.8 eV.

Photoelectrochemical Measurements.

Photoelectrochemical performances of the $BiVO_4$ and Ln-$BiVO_4$ electrodes used in this paper were evaluated in an undivided three-electrode configuration using an SP-200 potentiostat/EIS (BioLogic Science Instruments). Simulated solar light was obtained from a 300 W Xe arc lamp (Ushio America, Inc.), first passing through a water filter (IR filter), neutral density filters, and an AM1.5G filter. The light then passed through a fused silica fiber optic cable (Newport Instruments) and a collimating lens before reaching the sample (Newport) to achieve uniform light illumination. The samples were illuminated through the back (glass) side of the FTO substrate. The power density of the incident light was calibrated to 100 mW/cm^2 at the surface of the electrode backside, after the light passes through the FTO substrate, using a research radiometer (International Light, IL 1700) coupled to a thermopile detector (International Light, SED 623/HNK 15). The light spectrum was calibrated to match that of the solar spectrum using an NREL certified Si reference cell (Photo Emission Tech, Inc.).

Photoelectrochemical measurements were performed in 0.5 M potassium phosphate (KH_2PO_4) buffer solution at pH 7.3, with or without sodium sulfite as a hole scavenger. J-V performance under illumination was measured by sweeping the potential to the positive direction from the open circuit potential under illumination with a sweep rate of 10 mV/s. All measurements were carried out using a Pt counter electrode and Ag/AgCl reference electrode (4 M sat. KCl), though all results are presented against the reversible hydrogen electrode (RHE) for ease of comparison against the water oxidation and reduction potentials at the specified pH. The potential was converted from Ag/AgCl to RHE using the following equation.

$$E\ (\text{vs. RHE}) = E\ (\text{vs. Ag/AgCl}) + E_{Ag/AgCl}\ (\text{reference}) + 0.0591\ V \times pH$$

$$(E_{Ag/AgCl}\ (\text{reference}) = 0.1976\ V \text{ vs. NHE at } 25\ ^{o}C)$$

Capacitance measurements for Mott-Schottky plots were obtained using the same aforementioned three electrode cell configuration and SP-200 potentiostat/EIS (BioLogic Science Instrument). The measurements were taken in a 0.5 M potassium phosphate (KH_2PO_4) buffer solution at pH 7.3. A sinusoidal modulation of 10 mV was applied at frequencies of 0.5 and 1 kHz. All electrodes were masked to the same geometric area of ~0.2 cm^2 for this measurement.

Electronic Structure Calculations.

Spin-polarized density-functional theory (DFT)[28] calculations were performed using plane-wave basis sets with the Quantum ESPRESSO package.[29] We used exchange-correlation functionals within the Perdew-Burke-Ernzerhof generalized gradient approximation (PBE)[30] and pseudopotentials within the projector-augmented wave (PAW) method.[31-33] We included Hubbard *U*-corrections to the *d* electrons of V, U(V)=2.7 eV as used in previous studies,[15, 21], and to the *f* electrons of the lanthanide atoms, U(Ln)=5.0 eV, which is in the range of 2.5--5.5 eV suggested, e.g. by Topsakal et al.[33] We used a (2x1x2) supercell of $BiVO_4$ with 96 atoms; one Bi atom of the supercell was replaced with a Ln atom, corresponding to a doping concentration of 6.25% at the Bi site. The effects of O vacancies were also considered in our calculations; we simulated the O vacancies by removing one O atom from the supercell, which correspond to a defect concentration of ~1.56%. A (5x6x6) Monkhorst-Pack k-point grid was employed to sample the Brillouin zone.

3. Results and Discussion

Experimental results and discussions.

Nanoporous $BiVO_4$ electrodes used in this study were synthesized using a previously reported method where electrodeposited BiOI films were used as precursor films.[7] A typical SEM image of the BiOI films used for the synthesis is shown in Figure 1a. BiOI films were converted to $BiVO_4$ electrodes by covering the electrode with a DMSO solution containing vanadyl acetylacetonate as the vanadium source and heating it at 450 °C in the air. Unreacted vanadium ions that formed V_2O_5 on the $BiVO_4$ surface could be easily removed by immersing the film in 1 M NaOH for 30 minutes.

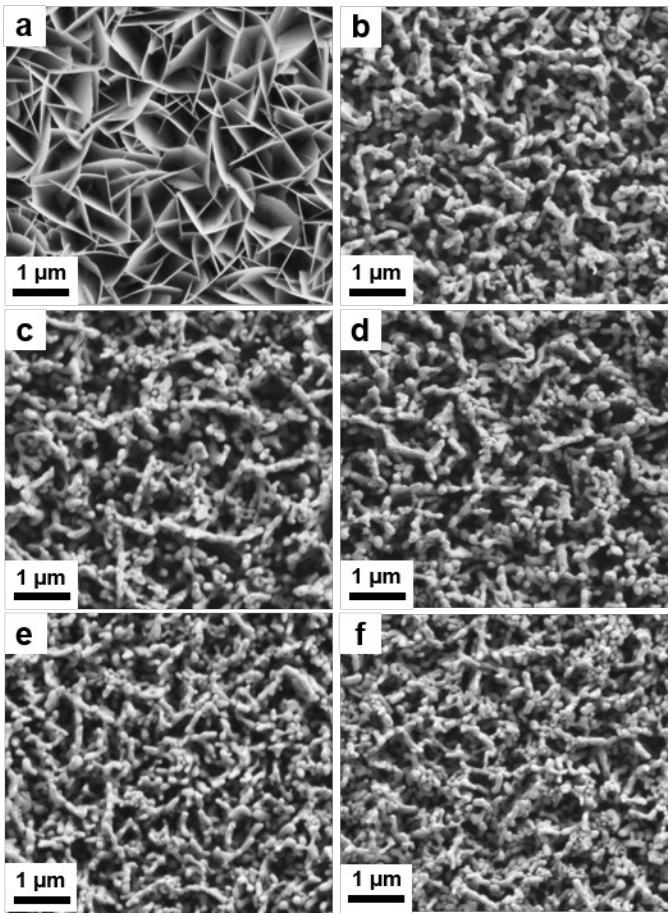

Figure 1. SEM images of (a) BiOI, (b) pristine $BiVO_4$, (c) La-doped $BiVO_4$, (d) Ce-doped $BiVO_4$, (e) Sm-doped $BiVO_4$, and (f) Yb-doped $BiVO_4$.

This synthesis method also allowed for the preparation of Ln-doped $BiVO_4$ electrodes by simply adding the lanthanide of interest (La, Ce, Sm, and Yb) as part of the vanadium solution

used to convert BiOI to $BiVO_4$. The concentration of lanthanide ions in the vanadium solution was varied to result in Ln-doped $BiVO_4$ electrodes where the content of Ln (mol of Ln/mol of (Bi+Ln) is 0.025-0.030. (In other words, 2.5-3% Bi in the Bi sites is replaced by Ln ions.) The content of Ln ions in doped $BiVO_4$ samples were determined using energy dispersive X-ray spectroscopy (EDS).

This synthesis method ensured that the morphology and particle size of the pristine and doped $BiVO_4$ electrodes are comparable (Figure 1b-f). This enabled us to assume that lanthanide doping is solely responsible for the difference observed in any properties or performances between pristine and doped $BiVO_4$ electrodes.

The fact that the lanthanide ions indeed substitutionally replaced Bi^{3+} in the $BiVO_4$ lattice could be confirmed by comparing XRD patterns of pristine and doped $BiVO_4$ films (Figure 2a). The addition of all lanthanide dopants did not change the overall monoclinic crystal structure of $BiVO_4$ or generate impurity peaks. However, close analysis of the X-ray patterns showed that Bragg peaks of $BiVO_4$ shifted to higher two theta values, which corresponds to a decrease in lattice parameters, upon doping. This is expected for substitutional replacement of Bi^{3+} ions with Ln^{3+} ions because Ln^{3+} ions are smaller than Bi^{3+} ions. (If Ln^{3+} is present in the interstitial sites or replaces V^{5+}, a decrease in cell parameters cannot be expected.) The trend for the shift to higher two theta values also matched very well with the size trend in the Ln^{3+} ions. La^{3+} and Ce^{3+}, which possess ionic radii that are only slightly smaller than Bi^{3+} (1.16 Å and 1.14 Å compared to 1.17 Å, respectively) showed a relatively small change in lattice parameters upon doping. Conversely, Sm^{3+} and Yb^{3+} possess ionic radii much smaller than that of La and Ce (1.08 Å and 0.98 Å, respectively) and correspondingly showed a larger decrease in lattice parameters and peak positions. The shifts of (1-12) and (004) peaks appearing at two theta values of 28.9° and 30.5°,

respectively, are shown as examples in Figure 2b. These results unambiguously confirm that the Ln doping resulted in the replacement of Bi^{3+} ions with Ln^{3+} ions.

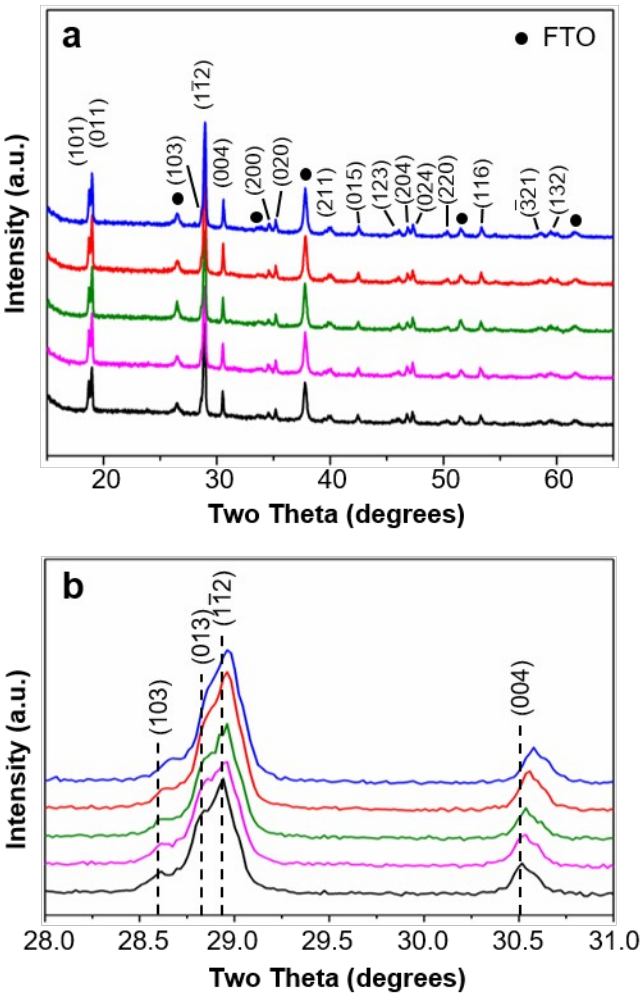

Figure 2. (a) XRD patterns of pristine (black) and doped $BiVO_4$: La (pink), Ce (green), Sm (red), and Yb (blue). Peaks were indexed according to JCPDS card 83-1699. (b) Magnified spectra showing the shifts of a few selected Bragg peaks.

The UV-visible absorbance spectra for the Ln-doped $BiVO_4$ show that Ln doping induced little change in light absorption of $BiVO_4$ (Figure 3). The major bandgap transition is seen to begin at ~520 nm in all lanthanide-doped samples and pristine $BiVO_4$. However, in the case of Ce-doped $BiVO_4$, an absorption tail below the bandgap energy exists, suggesting the presence of interband states in the bandgap region. Photoelectrochemical properties of this sample, which are

discussed below, show that this interband absorption did not contribute to an increase in photocurrent.

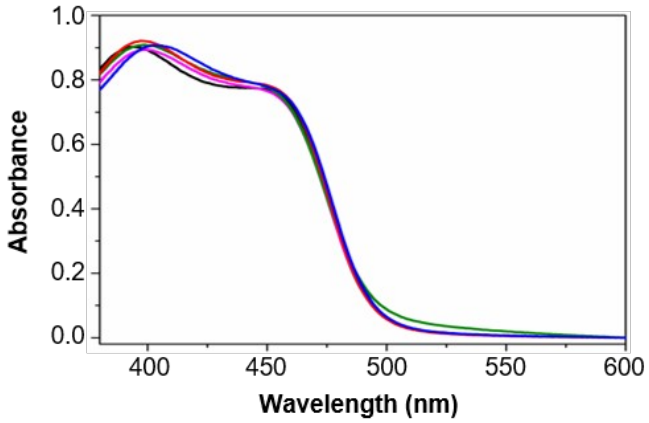

Figure 3. UV-visible absorbance spectra of pristine (black) and doped $BiVO_4$: La (pink), Ce (green), Sm (red), and Yb (blue).

The current density-potential (J-V) characteristics of the Ln-doped films were examined and compared to that of pristine $BiVO_4$ using photooxidation of sulfite to probe the effects of doping on charge transport and electron-hole separation. Sulfite ion was employed as a hole scavenger because of its fast oxidation kinetics.[34] Since sulfite oxidation can consume almost all the surface reaching holes, any change in photocurrent density for sulfite oxidation after Ln doping can be directly related to the change in the number of surface-reaching holes or the yield for electron-hole separation.

The J-V plots in Figure 4a show that Ce doping is detrimental to photocurrent generation of $BiVO_4$. La doping also resulted in a decrease in photocurrent generation although the decrease is not as considerable as that caused by Ce doping. Conversely, Sm and Yb doping slightly enhanced the photocurrent.

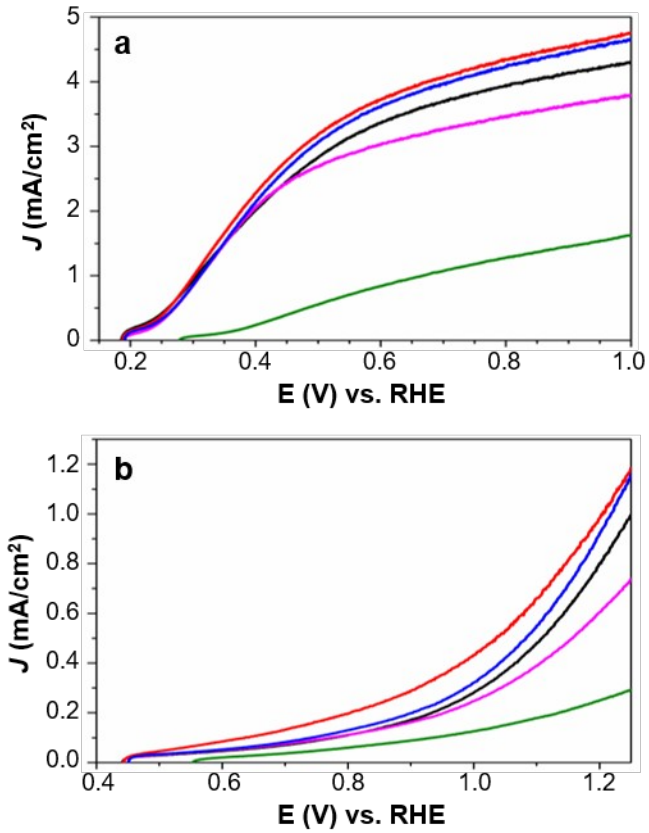

Figure 4. (a) J-V plots for sulfite oxidation under AM 1.5G, 100 mW/cm^2 illumination for undoped (black) and doped $BiVO_4$ samples: La (pink), Ce (green), Sm (red), and Yb (blue). The measurement was performed in 0.5 M phosphate buffer (pH 7.3) containing 1 M Na_2SO_3 using a scan rate of 10 mV/s. (b) J-V plots for water oxidation obtained in 0.5 M phosphate buffer (pH 7.3). The average photocurrent densities with standard deviations obtained with five different samples for each case can be found in Tables S1-2.

The J-V plots were also measured for photooxidation of water (Figure 4b). Since water oxidation kinetics are poor on the $BiVO_4$ surface, the photocurrent obtained for water oxidation was generally lower than that of sulfite oxidation for all samples. However, a nearly identical trend for photocurrent generation due to the dopants was observed for water oxidation as was seen for sulfite oxidation. This suggests that any of the Ln dopants is not particularly catalytic for water oxidation and the trend of photocurrent for water oxidation was mainly affected by Ln dopants altering charge transport and electron-hole recombination in $BiVO_4$.

In order to investigate the effect of Ln doping on the majority carrier concentration of $BiVO_4$, Mott-Schottky plots of pristine and doped $BiVO_4$ electrodes were obtained at two different frequencies in 0.5 M phosphate buffer (pH 7.3) (Figure 5 and Table S3). As the $BiVO_4$ electrodes used in this study have nanoporous morphologies and their true surface areas are not known, accurate determination of the carrier density of these electrodes was not possible. However, since all of the doped and pristine samples have comparable morphologies and surface areas, the change in slope of the Mott-Schottky plots could still be used to qualitatively compare carrier densities of these electrodes.

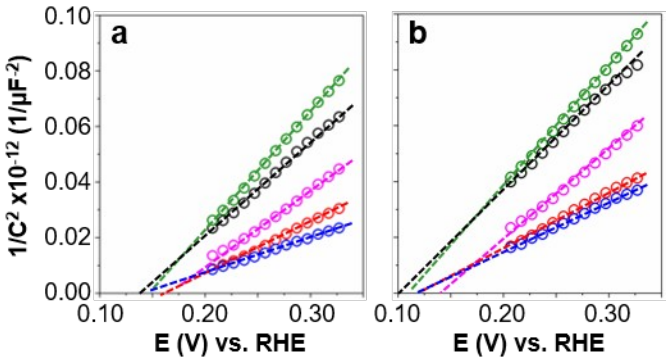

Figure 5. Mott-Schottky plots for pristine (black) and doped $BiVO_4$ (La (pink), Ce (green), Sm (red), and Yb (blue)) measured in 0.5 M phosphate buffer at two different frequencies, (a) 0.5 kHz and (b) 1 kHz. The average slopes with standard deviations obtained with five different samples for each case can be found in Table S3.

The results show a slight frequency dependence but the trends shown in each frequency are consistent. The La- and Ce- doped samples show slopes that are similar to those of pristine $BiVO_4$. This means that the decreased photocurrent observed with La and Ce-doped samples are not due to a decrease in carrier density but due to other effects. The Sm- and Yb-doped samples show slopes that are approximately half of the slopes observed in the pristine sample (Table S3). This suggests that the enhanced photocurrent observed with Sm- and Yb-doped samples are related to an increase in carrier density in these samples.

The oxidation states of the dopants as well as any changes in the oxidation state of the host elements were examined by XPS, which are critical to understand the doping effects. In all lanthanide-doped samples, the positions of the Bi 4f peaks and V 2p peaks were all found to be unchanged relative to pristine samples within the instrument error of 0.1 eV (Supplementary Figure S1). This suggests that Ln doping did not considerably affect the oxidation states and bonding environments of the Bi^{3+} and V^{5+} ions.

The La 3d peaks of the La-doped $BiVO_4$ are shown in Figure 6a. These peak positions (835.6 eV for $3d_{5/2}$ and 839.2 eV for $3d_{3/2}$) match very well with those of La^{3+} in La_2O_3, confirming the presence of La only in the +3 oxidation state in the Ln-doped $BiVO_4$ lattice.[35-36] The Ce 3d peaks of the Ce-doped $BiVO_4$ show doublets for both $3d_{5/2}$ (881.7 eV and 885.5 eV) and $3d_{3/2}$ peaks (900.2 eV and 904.3 eV), which are typical peak shapes and positions expected for Ce^{3+} (Figure 6b).[24, 37] The Ce 3d peaks of CeO_2, which contains only Ce^{4+} are also shown for comparison. Ce^{4+} peaks are composed of multiplets for both $3d_{5/2}$ and $3d_{3/2,}$ which overlap with doublets for $3d_{5/2}$ and $3d_{3/2}$ of Ce^{3+}. Therefore, easy differentiation of Ce^{4+} and Ce^{3+} peaks may be difficult. However, a peak appearing at 917 eV can be used as an unambiguous indication for the presence of Ce^{4+} ions.[37] Therefore, the lack of a Ce^{4+} peak at 917 eV in the spectrum of the Ce-doped sample confirms that Ce dopants in the Ce-doped $BiVO_4$ are all stabilized in the +3 oxidation state.

The fact that both La and Ce dopants are present in the 3+ oxidation states confirm that substitutional La and Ce doping on Bi sites are isovalent doping and, therefore, a change in majority carrier density of $BiVO_4$ is not expected. This result agrees well with the result obtained by the Mott-Schottky plots. This also means that the decrease in photocurrent obtained with La and Ce-doped samples is not due to the carrier concentration change but through other

mechanisms such as change in mobility or the presence of interband states affecting electron-hole recombination.

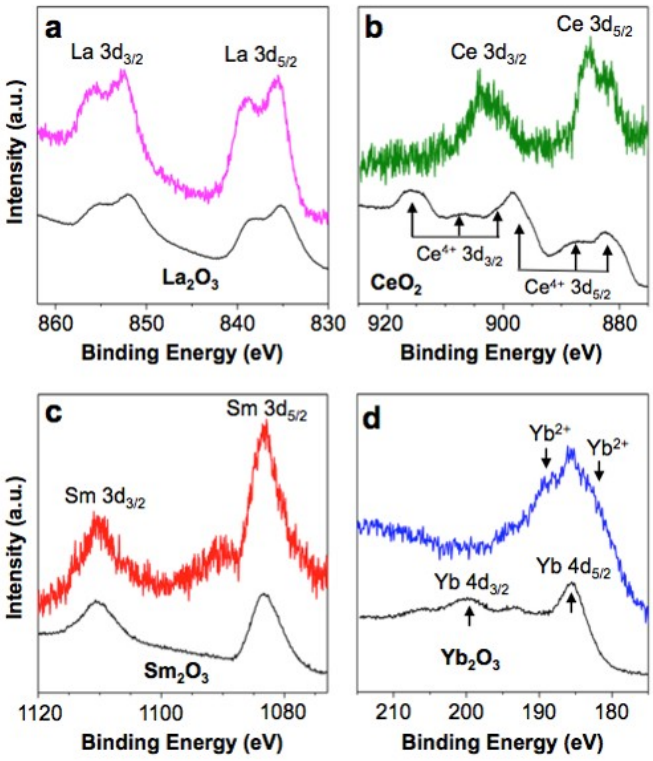

Figure 6. XPS of (a) La 3d peaks in La-doped $BiVO_4$ (pink) and in La_2O_3 (black), (b) Ce 3d peaks in Ce-doped $BiVO_4$ (green) and CeO_2 (black). (c) Sm 3d peaks in Sm-doped $BiVO_4$ (red) and Sm_2O_3 (black), and (d) Yb 4d peaks in Yb-doped $BiVO_4$ (blue) and Yb_2O_3 (black).

The Sm 3d peak of the Sm-doped $BiVO_4$ appeared at 1083.1 eV and 1109.8 eV, which are major peaks of $3d_{5/2}$ and $3d_{3/2}$, respectively (Figure 6c). The positions and shapes of these peaks match well with those of Sm^{3+} in Sm_2O_3 used as a reference. There is an additional peak appearing at 1090.7 eV only with the Sm-doped sample. This peak, which is known as an energy loss satellite peak of $3d_{5/2}$, is also associated with +3 oxidation state of Sm.[38] The presence of Sm^{2+} in the Sm-doped sample is unlikely because of the absence of characteristic peaks for Sm^{2+} that are reported to appear at ~1074 eV and ~1096 eV in the literature.[39-41] Therefore, it was concluded that Sm ions in the Sm-doped sample are present as Sm^{3+}, meaning that Sm doping is

also isovalent doping. As mentioned above, isovalent doping cannot change the majority carrier density. Therefore, the discrepancy between the Mott-Schottky results and XPS results suggests that Sm doping most likely affected other features of $BiVO_4$, such as the concentration of oxygen vacancies, to alter the charge carrier density of $BiVO_4$ and enhance photocurrent.

In the case of Yb-doped $BiVO_4$, however, both Yb^{3+} and Yb^{2+} ions appear to be present. For Yb_2O_3, which contains only Yb^{3+} ions, the two most intense peaks associated with 4d electrons are found at 185.3 eV and 199.5 eV, which are attributed to the $4d_{5/2}$ and $4d_{3/2}$ spin states, respectively.[42] These peaks each have shake-up lines that are found at ~193.2 eV and 206.0 eV, about 6-7 eV higher than the main spin state features. Compared to the $4d_{5/2}$ peak of Yb_2O_3, the $4d_{5/2}$ peak of the Yb-doped sample shows two shoulder peaks at 181.8 eV and 189.7 eV, which are unlikely to be associated with the Yb^{3+} oxidation state. Although we were unable to find $4d_{5/2}$ peaks of Yb^{2+} stabilized in the oxide matrix reported in the literature, we note that there are reports of $4d_{5/2}$ peaks of Yb^{2+} at ~181.5 eV and ~190.1 eV in intermetallic compounds containing the Yb^{2+} oxidation state.[43-45] Therefore, these shoulder peaks may indicate the presence of Yb^{2+} ions in the Yb-doped sample. However, it is not certain whether the presence of Yb^{2+} is directly related to the observed carrier density increase of the Yb-doped sample. Therefore, DFT calculations were performed to construct electronic band structures of Ln-doped $BiVO_4$ so that the relationship between Ln-doping and all the aforementioned experimental results can be further elucidated.

DFT calculations on Ln Doping.

Results for La doping. For La-doped $BiVO_4$ we found that the presence of La atoms does not affect the band structure of the system, as shown in Figure S2; we obtained an indirect band gap of ~2.31 eV for La-$BiVO_4$ similar to the band gap computed for pristine $BiVO_4$ (~2.27 eV);

the slight increase in the band gap is due to a minor downward shift of the valence band minimum (VBM). However, this change is negligible and we do not expect it will be responsible for a difference in photon absorption, as shown in Figure 3. We note that the major electronic state contributions from the La dopant are located deep in the conduction band, far from the band edges and the band gap region (see Figure S2). Therefore, the decrease in photocurrent observed experimentally in the La-doped samples cannot be explained using only the results of the La doped band energies.

In order to examine whether La doping affected the mobilities of charge carriers, we computed the effective masses of holes and electrons in pristine and La-doped $BiVO_4$, as well as in the other doped systems. The effective masses were computed from quadratic fits of the bands. We found significant increases in the effective masses of both electrons and holes in La- and Ce-doped $BiVO_4$. For example, the effective mass of holes was found to increase by 24% (33%) in La-(Ce-) doped $BiVO_4$ compared to that of the pristine system. The presence of heavier carriers in La-$BiVO_4$ and in Ce-$BiVO_4$ may be one of the reasons for the reduced photocurrent observed in these systems. We found that the effective masses of carriers in Yb- and Sm-$BiVO_4$ are also slightly heavier than those of pristine $BiVO_4$, although lighter than those in La- and Ce-$BiVO_4$ (see Table S4).

Results for Ce doping. For Ce-doped $BiVO_4$ we found an indirect band gap of ~2.30 eV, almost the same as that of pristine $BiVO_4$. Overall, the band structure of Ce-doped $BiVO_4$ was found to be similar to that of pristine $BiVO_4$ (see Figure 7(a)), except for an occupied state in the gap, at about 0.5 eV above the VBM. The filled state in the midgap region, which is mainly composed of Ce f orbitals (Fig. 7(b)), may act as a recombination center when electron-hole pairs are generated: when holes are generated in the valence band, they may recombine with

electrons occupying the midgap state, which, if left empty, may then be filled by an electron initially excited to the conduction band. The net effect is a recombination process involving the mid-gap state, which is one of possible processes explaining the reduced photocurrent observed in the Ce-doped samples.

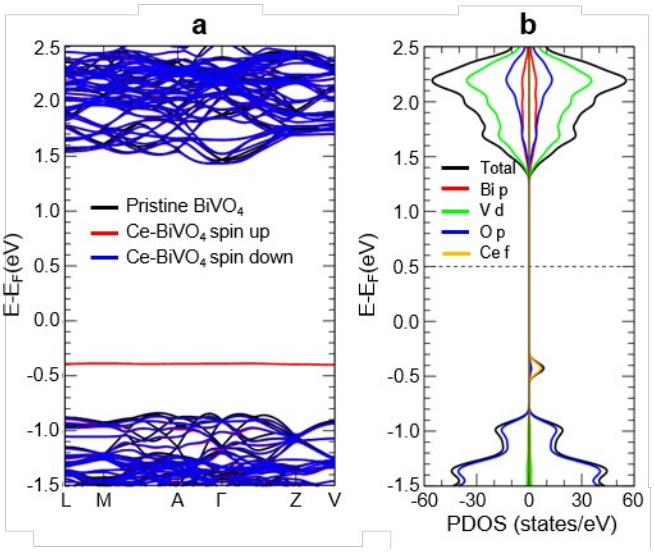

Figure 7. (a) Band structures of pristine and Ce-doped $BiVO_4$; the band structures were aligned using the position of the *3s* energy levels of a V atom located far from the dopant and the reference energy was set at the Fermi level of the doped system. (b) Projected density of states (PDOS) of Ce-doped $BiVO_4$, spin up in the right panel and spin down in the left panel. Note that the spin-up and spin-down state are indistinguishable in our calculations and both spin-up and spin-down states are present in the real material.

We note that our results showing the formation of a filled state in the midgap region in the presence of Ce doping are consistent with those previously reported by Jiang et al.[24] However, while our experimental results show a photocurrent decrease by Ce doping, Jiang at al. reported a photocurrent enhancement by Ce doping.[24] As we mentioned previously, doping may lead to different outcomes if it is accompanied by changes in morphology, surface area, and crystallinity of the host material. The effect of Ce doping can be explicitly and accurately determined only when it is achieved without changing other materials properties. Our SEM and

XRD results confirmed that the Ce doping in our samples was achieved without inducing a change in morphology and crystallinity and that Ce was truly incorporated into the $BiVO_4$ lattice.

We also found that holes and electrons in Ce-doped $BiVO_4$ have the largest effective masses among all the doped systems considered here. As shown in Table S4, the effective masses of holes (electrons) increase by 33% (11%) in Ce-doped $BiVO_4$ compared to those of pristine $BiVO_4$. These results point at lower carrier mobilities in Ce-doped $BiVO_4$ when compared to those of other systems investigated here, which may be one of the reasons for the reduced photocurrent measured in the Ce-doped samples.

Results for Sm and Yb doping. For both Yb-doped and Sm-doped $BiVO_4$ we found indirect band gaps of ~2.3 eV (similar to the band gap of pristine $BiVO_4$) and no significant shifts in the valence and conduction band edges with respect to those of the pristine system (see Figs. 8(a) and 9(a)). In both systems we found unoccupied states in the band gap region: in Yb-$BiVO_4$ (Fig. 8) we observed the presence of an isolated empty band at about 1.5 eV below the conduction band minimum (CBM), mainly composed of Yb *f* states; in Sm-$BiVO_4$ (Fig. 9) we found two unoccupied bands between 0.4 and 0.9 eV below the CBM, which mainly originate from Sm *f* states. However, the presence of these empty interband states in the midgap region cannot explain the enhanced photocurrent or the increased carrier concentration of Yb- and Sm-doped samples. We then turned to study possible effects originating from the combined presence of dopants and oxygen vacancies.

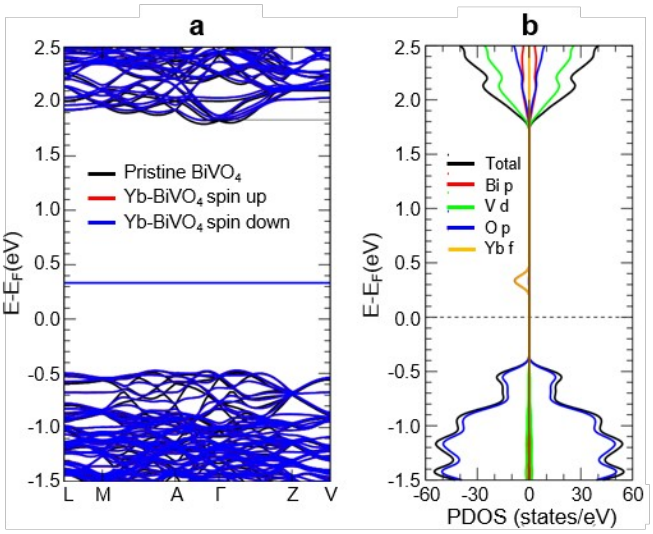

Figure 8. (a) Band structures of pristine and Yb-doped $BiVO_4$; the band structures were aligned using the position of the *3s* energy levels of a V atom located far from the dopant and the reference energy was set at the Fermi level of the doped system. (b) Projected density of states (PDOS) of Yb-doped $BiVO_4$, spin up in the right panel and spin down in the left panel.

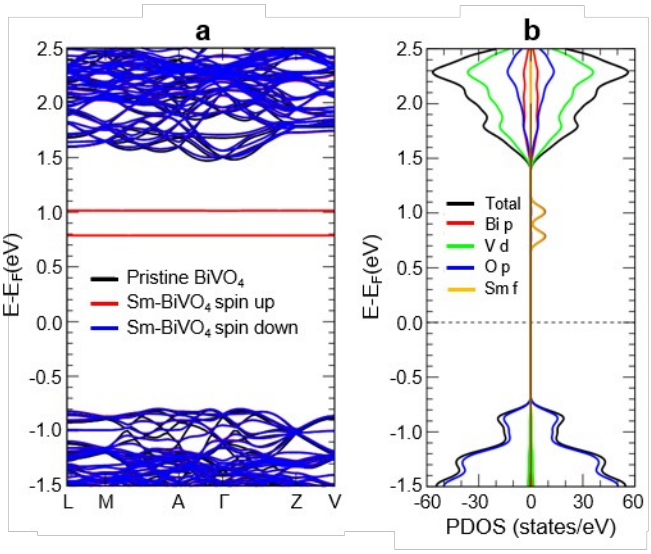

Figure 9. (a) Band structures of pristine and Sm-doped $BiVO_4$; the band structures were aligned using the position of the *3s* energy levels of a V atom located far from the dopant and the reference energy was set at the Fermi level of the doped system. (b) Projected density of states (PDOS) of Sm-doped $BiVO_4$, spin up in the right panel and spin down in the left panel.

DFT calculations on the combined effect of Ln Doping and O vacancy. Oxygen vacancy is an intrinsic defect in $BiVO_4$ and may interact with extrinsic Ln dopants. For example, a joint theoretical and experimental study recently showed that the combined effect of nitrogen doping

and the generation of O vacancies can improve the performance of $BiVO_4$ for solar water splitting.[21] Therefore, we investigated the interaction of Ln doping and O vacancy. We considered one Ovacancy in a supercell with 96 atoms (64 O atoms), which corresponds to a concentration of ~1.56%. In pristine $BiVO_4$ (Fig. S3), we found that the presence of O vacancy leads to the formation of a localized filled state in the midgap region, at ~1.4 eV above the VBM; no changes in the band gap and in the band edge positions were observed, in agreement with our previous study (Figure 10a-b).[21] For both La- and Ce-doped $BiVO_4$ we found that combining O vacancy with doping resulted in a straightforward addition of the two effects, with no interaction or synergy among them (see Figure S3).

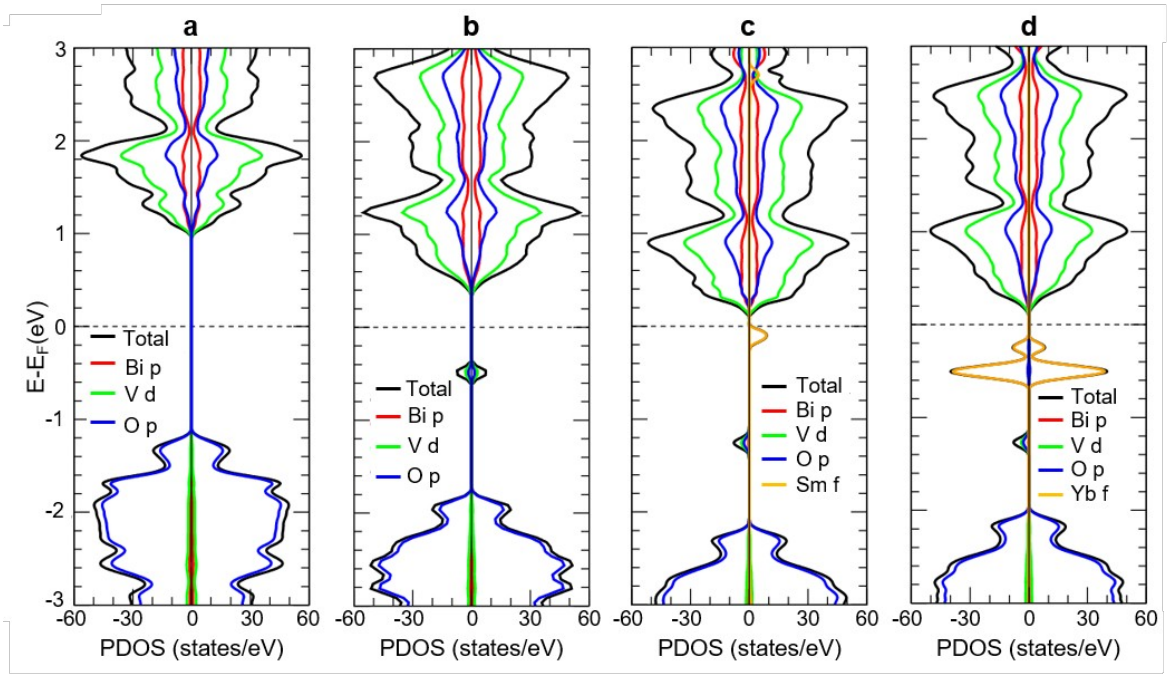

Figure 10. Projected density of states (PDOS) of (a) pristine $BiVO_4$, (b) $BiVO_4$ with O vacancy, (c) Sm-doped $BiVO_4$ with O vacancy and (d) Yb-doped $BiVO_4$ with O vacancy. Spin up in the right panel and spin down in the left panel.

Interestingly, when an O vacancy was combined with Sm or Yb doping, the resulting band structure was more complex (Figure 10c-d). The empty midgap states observed in the case

of Sm or Yb doping alone are no longer present, and new filled midgap states are present near the CBM, which may serve as donor states (Figure 10c-d). These filled states have mainly a lanthanide *f* character and are located between 0.3 and 1.0 eV below the CBM in Yb-doped $BiVO_4$, and between 0.1 and 0.3 eV below the CBM in Sm-doped $BiVO_4$. We also found additional filled states with oxygen character, positioned lower in energy, relative to the CBM, than the *f* lanthanide states (Figure 10c-d). These states are also lower in energy than the filled midgap state formed by O vacancy alone (Figure 10b).

These results suggest that although Sm or Yb doping alone does not provide donor states and hence does not increase carrier densities, the combination of Sm or Yb doping with O vacancies may give rise to donor states that are different from those formed by O vacancies alone. In particular, these states are closer to the CBM and hence, in principle, easier to ionize; thus they may be responsible for the higher carrier density shown in the Mott-Schottky plots as well as for the enhanced photocurrent caused by Sm and Yb doping. Although further investigations are necessary to come to definitive conclusions, including a study of polarons in the doped material, our results on the electronic states clearly demonstrate the effect of the interaction of intrinsic defects, in particular oxygen vacancies, and extrinsic dopants.

Conclusions

In summary, we found that substitutional doping at the Bi^{3+} site with La, Ce, Sm, and Yb resulted in several unique changes in the photoelectrochemical properties of $BiVO_4$. Enhancements in the photoelectrochemical oxidation of sulfite and water were found in the cases of Sm and Yb and the opposite effect was observed in the case of La and Ce. These effects can be explained by changes in the electronic structure of the doped $BiVO_4$ compared to the pristine

one, as elucidated by DFT calculations. La doping was found to decrease the performance due, at least in part, to a significant increase in the effective masses of electrons and holes, thus leading to a possible decrease in carrier mobilities of $BiVO_4$. Ce doping was found to severely limit the performance of the material, due to the combined effect of increased effective masses of electrons and holes and the formation of a filled midgap state near the VBM, which likely acted as a recombination center for photogenerated electron-hole pairs. Sm and Yb doping led instead to an increase in carrier density which was interpreted as arising from donor states present below the CBM, which were found in DFT calculations when both dopants and oxygen vacancies were considered to coexist in the sample. The donor states obtained by the simultaneous consideration of Sm/Yb doping and O vacancy, which was critical for the interpretation of the experimental results, could not be obtained by the simple addition of the changes caused by Sm/Yb doping alone and O vacancy alone. This understanding may serve as a useful guideline for studying doped oxides where O vacancies are known to be intrinsic, common defects.

Associated Content

Supporting Information

The Supporting Information is available free of charge on the ACS Publications website at DOI:

XPS, supplementary band structures, and tables summarizing changes caused by Ln doping in photocurrent generation, Mott-Schottky plots, and effective masses of electrons and holes.

Author Information

Corresponding Author

*Email: kschoi@chem.wisc.edu and gagalli@uchicago.edu

Acknowledgements

This work was supported by the National Science Foundation (NSF) under the NSF Center (CHE- 1305124). J.M.M. and G.A.G. acknowledge the use of computational resources at the Research Computing Center (RCC) at the University of Chicago.

References

1. Lewis, N. S.; Nocera, D. G., Powering the planet: Chemical challenges in solar energy utilization. *Proc. Natl. Acad. Sci. USA* **2006,** *103*, 15729-15735.

2. Li, Z.; Luo, W.; Zhang, M.; Feng, J.; Zou, Z., Photoelectrochemical cells for solar hydrogen production: current state of promising photoelectrodes, methods to improve their properties, and outlook. *Energy Environ. Sci.* **2013,** *6*, 347-370.

3. Pinaud, B. A.; Benck, J. D.; Seitz, L. C.; Forman, A. J.; Chen, Z.; Deutsch, T. G.; James, B. D.; Baum, K. N.; Baum, G. N.; Ardo, S.; Wang, H.; Miller, E.; Jaramillo, T. F., Technical and economic feasibility of centralized facilities for solar hydrogen production via photocatalysis and photoelectrochemistry. *Energy Environ. Sci.* **2013,** *6*, 1983-2002.

4. Sivula, K.; van de Krol, R., Semiconducting materials for photoelectrochemical energy conversion. *Nat. Rev. Mater.* **2016,** *1*, 15010.

5. Kang, D.; Kim, T. W.; Kubota, S. R.; Cardiel, A. C.; Cha, H. G.; Choi, K.-S., Electrochemical Synthesis of Photoelectrodes and Catalysts for Use in Solar Water Splitting. *Chem. Rev.* **2015,** *115*, 12839-12887.

6. Park, Y.; McDonald, K. J.; Choi, K.-S., Progress in bismuth vanadate photoanodes for use in solar water oxidation. *Chem. Soc. Rev.* **2013,** *42*, 2321-2337.

7. Kim, T. W.; Choi, K.-S., Nanoporous BiVO4 Photoanodes with Dual-Layer Oxygen Evolution Catalysts for Solar Water Splitting. *Science* **2014,** *343*, 990.

8. Abdi, F. F.; van de Krol, R., Nature and Light Dependence of Bulk Recombination in Co-Pi-Catalyzed BiVO4 Photoanodes. *J. Phys. Chem. C* **2012,** *116*, 9398-9404.

9. Berglund, S. P.; Flaherty, D. W.; Hahn, N. T.; Bard, A. J.; Mullins, C. B., Photoelectrochemical Oxidation of Water Using Nanostructured BiVO4 Films. *J. Phys. Chem. C* **2011,** *115*, 3794-3802.

10. Kuang, Y.; Jia, Q.; Nishiyama, H.; Yamada, T.; Kudo, A.; Domen, K., A Front-Illuminated Nanostructured Transparent BiVO4 Photoanode for >2% Efficient Water Splitting. *Adv. Energy Mater.* **2015,** *6*, 1501645.

11. Kudo, A.; Omori, K.; Kato, H., A Novel Aqueous Process for Preparation of Crystal Form-Controlled and Highly Crystalline BiVO4 Powder from Layered Vanadates at Room Temperature and Its Photocatalytic and Photophysical Properties. *J. Am. Chem. Soc.* **1999,** *121*, 11459-11467.

12. Kuang, Y.; Jia, Q.; Ma, G.; Hisatomi, T.; Minegishi, T.; Nishiyama, H.; Nakabayashi, M.; Shibata, N.; Yamada, T.; Kudo, A.; Domen, K., Ultrastable low-bias water splitting photoanodes via photocorrosion inhibition and in situ catalyst regeneration. *Nat. Energy* **2016,** *2*, 16191.

13. Lee, D. K.; Choi, K.-S., Enhancing long-term photostability of BiVO4 photoanodes for solar water splitting by tuning electrolyte composition. *Nat. Energy* **2018,** *3*, 53-60.

14. Berglund, S. P.; Rettie, A. J. E.; Hoang, S.; Mullins, C. B., Incorporation of Mo and W into nanostructured BiVO4 films for efficient photoelectrochemical water oxidation. *Phys. Chem. Chem. Phys.* **2012,** *14*, 7065-7075.

15. Park, Y.; Kang, D.; Choi, K.-S., Marked enhancement in electron-hole separation achieved in the low bias region using electrochemically prepared Mo-doped BiVO4 photoanodes. *Phys. Chem. Chem. Phys.* **2014,** *16*, 1238-1246.

16. Abdi Fatwa, F.; Firet, N.; van de Krol, R., Efficient BiVO4 Thin Film Photoanodes Modified with Cobalt Phosphate Catalyst and W-doping. *ChemCatChem* **2012,** *5*, 490-496.

17. Chen, L.; Toma Francesca, M.; Cooper Jason, K.; Lyon, A.; Lin, Y.; Sharp Ian, D.; Ager Joel, W., Mo-Doped BiVO4 Photoanodes Synthesized by Reactive Sputtering. *ChemSusChem* **2015,** *8*, 1066-1071.

18. Wang, G.; Ling, Y.; Lu, X.; Qian, F.; Tong, Y.; Zhang, J. Z.; Lordi, V.; Rocha Leao, C.; Li, Y., Computational and Photoelectrochemical Study of Hydrogenated Bismuth Vanadate. *J. Phys. Chem. C* **2013,** *117*, 10957-10964.

19. Cooper, J. K.; Scott, S. B.; Ling, Y.; Yang, J.; Hao, S.; Li, Y.; Toma, F. M.; Stutzmann, M.; Lakshmi, K. V.; Sharp, I. D., Role of Hydrogen in Defining the n-Type Character of BiVO4 Photoanodes. *Chem. Mater.* **2016,** *28*, 5761-5771.

20. Jang, J. W.; Friedrich, D.; Müller, S.; Lamers, M.; Hempel, H.; Lardhi, S.; Cao, Z.; Harb, M.; Cavallo, L.; Heller, R.; Eichberger, R.; van de Krol, R.; Abdi Fatwa, F., Enhancing Charge Carrier Lifetime in Metal Oxide Photoelectrodes through Mild Hydrogen Treatment. *Adv. Energy Mater.* **2017,** *7*, 1701536.

21. Kim, T. W.; Ping, Y.; Galli, G. A.; Choi, K.-S., Simultaneous enhancements in photon absorption and charge transport of bismuth vanadate photoanodes for solar water splitting. *Nat. Comm.* **2015,** *6*, 8769.

22. Quinonero, J.; Lana-Villarreal, T.; Gomez, R., Improving the photoactivity of bismuth vanadate thin film photoanodes through doping and surface modification strategies. *Appl. Catal., B* **2016,** *194*, 141-149.

23. Wang, M.; Che, Y.; Niu, C.; Dang, M.; Dong, D., Effective visible light-active boron and europium co-doped BiVO4 synthesized by sol-gel method for photodegradation of methyl orange. *J. Hazard. Mater.* **2013,** *262*, 447-455.

24. Jiang, Z.; Liu, Y.; Jing, T.; Huang, B.; Zhang, X.; Qin, X.; Dai, Y.; Whangbo, M.-H., Enhancing the Photocatalytic Activity of BiVO4 for Oxygen Evolution by Ce Doping: Ce3+ Ions as Hole Traps. *J. Phys. Chem. C* **2016,** *120*, 2058-2063.

25. Shan, L.; Liu, Y., Er3+, Yb3+ doping induced core-shell structured BiVO4 and near-infrared photocatalytic properties. *J. Mol. Catal. A: Chem.* **2016,** *416*, 1-9.

26. Wang, M.; Niu, C.; Liu, J.; Wang, Q.; Yang, C.; Zheng, H., Effective visible light-active nitrogen and samarium co-doped BiVO4 for the degradation of organic pollutants. *J. Alloys Compd.* **2015,** *648*, 1109-1115.

27. McDonald, K. J.; Choi, K.-S., A new electrochemical synthesis route for a BiOI electrode and its conversion to a highly efficient porous BiVO4 photoanode for solar water oxidation. *Energy Environ. Sci.* **2012,** *5*, 8553-8557.

28. Hohenberg, P.; Kohn, W., Inhomogeneous Electron Gas. *Phys. Rev.* **1964,** *136*, B864-B871.

29. Paolo, G.; Stefano, B.; Nicola, B.; Matteo, C.; Roberto, C.; Carlo, C.; Davide, C.; Guido, L. C.; Matteo, C.; Ismaila, D.; Andrea Dal, C.; Stefano de, G.; Stefano, F.; Guido, F.; Ralph, G.; Uwe, G.; Christos, G.; Anton, K.; Michele, L.; Layla, M.-S.; Nicola, M.; Francesco, M.; Riccardo, M.; Stefano, P.; Alfredo, P.; Lorenzo, P.; Carlo, S.; Sandro, S.; Gabriele, S.; Ari, P. S.; Alexander, S.; Paolo, U.; Renata, M. W., QUANTUM ESPRESSO: a modular and open-source software project for quantum simulations of materials. *J. Phys.: Condens. Matter* **2009,** *21*, 395502.

30. Perdew, J. P.; Burke, K.; Ernzerhof, M., Generalized Gradient Approximation Made Simple. *Phys. Rev. Lett.* **1996,** *77*, 3865-3868.

31. Standard Solid State Pseudopotentials (SSSP): Downloads. http://materialscloud.org/sssp/downloads.html (accessed May 14, 2015).

32. Rare Earth PAW datasets. http://www.vlab.msi.umn.edu/resources/repaw/index.shtml (accessed May 14, 2015).

33. Topsakal, M.; Wentzcovitch, R. M., Accurate projected augmented wave (PAW) datasets for rare-earth elements (RE=La–Lu). *Comput. Mater. Sci.* **2014,** *95*, 263-270.

34. Sarala, R.; Islam, M. A.; Rabin, S. B.; Stanburg, D. M., Aromatic sulfonation by sulfite and the reduction potential of the sulfite radical: oxidation of sulfite by the tetraammine(phenanthroline)ruthenium(II) cation. *Inorg. Chem.* **1990,** *29*, 1133-1142.

35. Sarma, D. D.; Hegde, M. S.; Rao, C. N. R., Study of surface oxidation of rare-earth metals by photoelectron spectroscopy. *J. Chem. Soc. Faraday Trans. 2: Mol. & Chem. Phys.* **1981,** *77*, 1509-1520.

36. Zhang, J.; Wong, H.; Kakushima, K.; Iwai, H., XPS study on the effects of thermal annealing on CeO2/La2O3 stacked gate dielectrics. *Thin Solid Films* **2016,** *600*, 30-35.

37. Mullins, D. R.; Overbury, S. H.; Huntley, D. R., Electron spectroscopy of single crystal and polycrystalline cerium oxide surfaces. *Surf. Sci.* **1998,** *409*, 307-319.

38. Dufour, G.; Karnatak, R. C.; Mariot, J. M.; Bonnelle, C., Atomic and chemical effects in Sm and Sm2O3 photoelectron spectra. *Chem. Phys. Lett.* **1976,** *42*, 433-436.

39. Krill, G.; Amamou, A.; Senateur, J. P., Valence changes of samarium ions in mixed SmS 1-x P x compounds studied by photoemission (XPS and UPS). *J. Phys. F* **1980,** *10*, 1889.

40. Mason, M. G.; Lee, S. T.; Apai, G.; Davis, R. F.; Shirley, D. A.; Franciosi, A.; Weaver, J. H., Particle-Size-Induced Valence Changes in Samarium Clusters. *Phys. Rev. Lett.* **1981,** *47*, 730-733.

41. Yamasaki, A.; Imada, S.; Higashimichi, H.; Fujiwara, H.; Saita, T.; Miyamachi, T.; Sekiyama, A.; Sugawara, H.; Kikuchi, D.; Sato, H.; Higashiya, A.; Yabashi, M.; Tamasaku, K.; Miwa, D.; Ishikawa, T.; Suga, S., Coexistence of Strongly Mixed-Valence and Heavy-Fermion Character in SmOs4Sb12 Studied by Soft- and Hard-X-Ray Spectroscopy. *Phys. Rev. Lett.* **2007,** *98*, 156402.

42. Reitz, C.; Haetge, J.; Suchomski, C.; Brezesinski, T., Facile and General Synthesis of Thermally Stable Ordered Mesoporous Rare-Earth Oxide Ceramic Thin Films with Uniform Mid-Size to Large-Size Pores and Strong Crystalline Texture. *Chem. Mater.* **2013,** *25*, 4633-4642.

43. Chung, J.-S.; Cho, E.-J.; Oh, S. J., 3d core-level photoemission spectra of intermetallic Yb compounds. *Phys. Rev. B* **1990,** *41*, 5524-5528.

44. Schmidt, S.; Hüfner, S.; Reinert, F.; Assmus, W., X-ray photoemission of YbInCu4. *Phys. Rev. B* **2005,** *71*, 195110.

45. Suga, S.; Ogawa, S.; Namatame, H.; Taniguchi, M.; Kakizaki, A.; Ishii, T.; Fujimori, A.; Oh, S.-J.; Kato, H.; Miyahara, T.; Ochiai, A.; Suzuki, T.; Kasuya, T., XPS and UPS Studies of Valence Fluctuation and Surface States of Yb4As3, Yb4Sb3 and Yb4Bi3. *J. Phys. Soc. Jpn.* **1989,** *58*, 4534-4543.